Logically Orthogonal Meshes for Geophysical Applications

Rowan Cockett and Eldad Haber
Department of Earth and Ocean Science
University of British Columbia
rcockett@eos.ubc.ca

Abstract

The use of a logically orthogonal mesh allows for alignment to features such as topography as well as a variety of new ways to pad the computational domain. The mesh presented has the potential to reduce the number of cells necessary as well as increase accuracy, for example, when topography plays an important role. These potential gains in computation motivate the investigation into writing discrete operators for these meshes. Two model geophysical problems are used as examples for implementing and testing the logically orthogonal mesh. We use the DC resistivity problem to look at some of the computational gains possible when aligning the mesh to a known layer. A geophysical EM problem is used to as a preliminary investigation into mesh padding. We find that the logically orthogonal mesh can significantly reduce the number of cells necessary when the mesh is aligned to a layer. However, the complexity of the matrix system to be solved is increased, especially in the DC resistivity problem. More research into effective padding techniques is recommended as the simple algorithms presented for mesh generation do not optimize volume or aspect ratios of the mesh cells.

1 Introduction and Motivation

Discretization techniques are the most basic components for simulating differential equations. Finite volume and finite element techniques allow you to subdivide your continuous differential equations onto discrete domains. As such, the knowledge and appropriate application of these methods is fundamental to simulating physical processes. The most basic finite volume discretization involves regularly or variably spaced tensor product grids. However, in geophysical applications we are often only interested in a smaller region of full domain and these standard tensor product meshes require unnecessarily fine discretizations where high-accuracies are not necessary. The inadequacies of these simple discretizations often leads to methods of local mesh refinement through QuadTree or OcTree methods. Another discretization technique is the use of logically orthogonal meshes that are not required to be on a Cartesian grid. These grids allow some level of local refinement but without the cost of unnecessary refinement outside areas of interest. Additionally, some of the refinements necessary can be alleviated by aligning the mesh to features of interest (e.g. topography). It is noted as well that these meshes can also be adaptively refined using OcTree methods, however, this is outside the scope of this paper.

Here we will review the theory and implementation of a finite volume discretization on a general logically orthogonal mesh in two- and three-dimensions. The resulting discretization will be lightly compared to a regular mesh through the use of several geophysical example problems, including DC resistivity, and Maxwell's equations. The main goal of this project is to create a general framework for working with finite volume problems such that switching meshes and PDEs is straight forward.

2 Background

In this paper we discretize a logically orthogonal mesh using a finite volume technique. For clarity, the terminology used is visually outlined in Figure 1. A three dimensional cell has 8 nodes, 12 edges, 6 faces, and one center. The

face and edge variables are vector quantities that are stored as magnitude only, the direction is in the positive grid direction as seen in Figure 1. For a general logically orthogonal mesh the locations of each node is stored, and the only requirement is non-intersecting cells with positive volumes. As such, in the general case both the edge and flux directions do not align with the Cartesian grid.

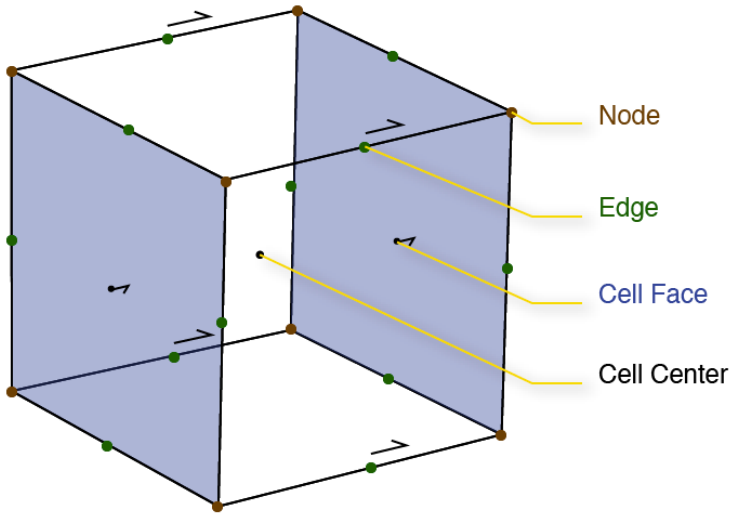

Figure 1: A single finite volume cell showing locations of variables.

3 Discretization

To guide the discretization on the logically orthogonal mesh, a few example problems will be used from geophysical methods. The DC resistivity problem, is a Poisson equation with a discontinuous conductivity model.

The equations for the DC resistivity problem are:

$$\begin{cases} \nabla \cdot \vec{J} = q \\ \sigma^{-1}\vec{J} = -\nabla\phi \end{cases} \tag{1}$$

Where J is the flux, σ is the electrical conductivity, ϕ is the electrical potential, and q is the source.

3.1 Divergence

The first equation (Eqn. 1) can be discretized by using the geometric interpretation of the divergence.

$$\int_V \nabla \cdot \vec{J}\, dV = \oint_{\partial V} (\vec{J}, \vec{n})\, dS \tag{2}$$

Where V is the volume, and $\vec{n}$ is the outward normal over the surface ∂V. Using this definition of the divergence on a standard finite volume discretization is straight forward, and can be applied to each cell in the domain.

As seen in Figure 2, the surface areas and normals of all cells in the mesh can be readily calculated. The flux values on each face $(\mathbf{J}_{(i)}, \mathbf{n}_{(i)})$ are discretized and represented by a scalar value. As such, these values need only be multiplied by the face area and multiplied by ± 1 to ensure an outward facing normal. To construct the divergence operator, **div**,

in one dimension the following distretization is used:

$$\mathbf{divj} = \mathbf{V}^{-1}\mathbf{D}_x\mathbf{A}\mathbf{j} = \ \mathsf{diag}\,(\mathbf{v})^{-1} \underbrace{\begin{bmatrix} -1 & 1 & & \\ & \ddots & \ddots & \\ & & -1 & 1 \end{bmatrix}}_{\mathbf{D}_x} \mathsf{diag}\,(\mathbf{a}) \begin{bmatrix} \mathbf{j}_1 \\ \mathbf{j}_2 \\ \vdots \\ \mathbf{j}_N \\ \mathbf{j}_{N+1} \end{bmatrix} = \mathbf{s} \tag{3}$$

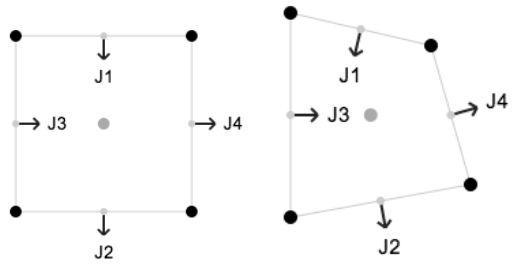

(a) Regular cell (b) Deformed cell

Figure 2: Fluxes into and out of a single cell on a regular and a deformed mesh.

Where $\mathbf{V}$ is a sparse matrix with the cell volumes on the diagonal, $\mathbf{D}$ is a difference matrix that ensures outward pointing normals, and $\mathbf{A}$ is a diagonal surface area matrix. To move to higher dimensions the logically-orthogonal structure is exploited, and Kronecker products may be used to place the difference matrix $\mathbf{D}$ on the correct cells. For example, the gradient matrix in three-dimensions may be formed by:

$$\mathbf{D}_x = \mathbf{I}_3 \otimes \mathbf{I}_2 \otimes \mathbf{D}_1$$
$$\mathbf{D}_y = \mathbf{I}_3 \otimes \mathbf{D}_2 \otimes \mathbf{I}_1 \tag{4}$$
$$\mathbf{D}_z = \mathbf{D}_3 \otimes \mathbf{I}_2 \otimes \mathbf{I}_1 \tag{5}$$

where $\mathbf{D}_n$ is the difference matrix in one-dimension for the n^{th} dimension. The $\mathbf{I}_n$ is the identity matrix that has the size of the mesh in the n^{th} dimension. Here the full divergence operator can be formed by:

$$\mathbf{div} = \mathbf{V}^{-1}[\mathbf{D}_x \quad \mathbf{D}_y \quad \mathbf{D}_z]\mathbf{A} \tag{6}$$

The divergence operator is easily created for this mesh because the position of the nodes is well defined. As such, the flux equation in the DC resistivity problem can be written in discrete form. The second equation, requires more detailed study as it is not trivial to separate the gradient operator into parts.

3.2 Face Inner Products

The standard approach for discretizing the gradient equation in Eqn. 1 is to isolate each component of the equation and integrate between cell centers.

$$\begin{aligned} \int_{x_{i,j}}^{x_{i+1,j}} \sigma^{-1} j^{(1)} dx &= \int_{x_{i,j}}^{x_{i+1,j}} \frac{\partial \phi}{\partial x} dx = \phi_{i+1,j} - \phi_{i,j} \\ \int_{y_{i,j}}^{y_{i,j+1}} \sigma^{-1} j^{(2)} dy &= \int_{y_{i,j}}^{y_{i,j+1}} \frac{\partial \phi}{\partial y} dy = \phi_{i,j+1} - \phi_{i,j} \end{aligned} \tag{7}$$

For the left hand side of Eqn. 7 careful attention must be paid to integrating a discontinuous conductivity between cells and the rectangular integration scheme for σ^{-1} can be used. This integration in the x component can be seen in Figure 3, and this simple illustration shows that breaking into components is not possible in the general case.

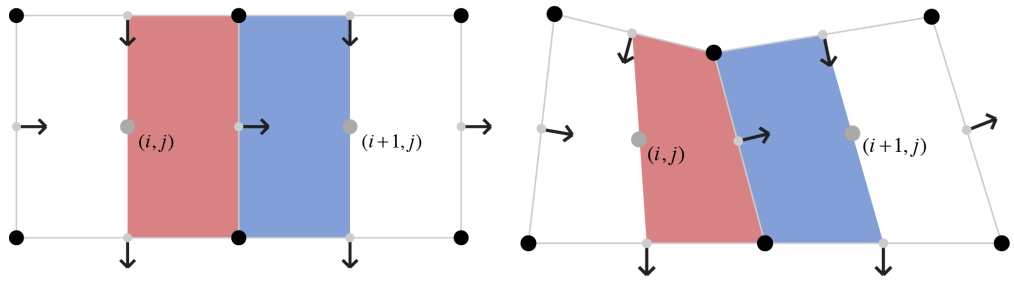

(a) Regular cell (b) Deformed cell

Figure 3: Integration over the first dimension of the mesh illustrates problems in the deformed case.

A more general methodology must be used to overcome coupling of component directions in the equation $\sigma^{-1}\vec{J} = \nabla\phi$. The equation is integrated with a general face function, $\vec{W}$, and the integral can be expanded using the fact that the gradient is the negative adjoint of the divergence operator [*Hyman et al.*, 2002].

$$\begin{aligned}\int_V (\sigma^{-1}\vec{J}, \vec{W})dV &= \int_V (\nabla\phi, \vec{W})dV \\ &= -\int_V \phi\nabla\cdot\vec{W}dV + \oint_{\partial V}\phi(\vec{W}, \vec{n})dS\end{aligned} \tag{8}$$

This allows us to discretize the gradient operator in terms of the divergence operator, which is well defined. The left hand side of this equation requires the inner product between two vectors; this operation is well defined in Cartesian coordinates but not on the deformed mesh. To discretize this face inner product, the flux on the faces of a cell must be translated to a single Cartesian vector ($\mathbf{j}_c$). The projection from Cartesian coordinates to the mesh coordinates is completed for every node of the mesh, and in 2D has the form:

$$\begin{aligned}\begin{bmatrix} j^{(1)} \\ j^{(3)} \end{bmatrix} &= \begin{bmatrix} n_x^{(1)} & n_y^{(1)} \\ n_x^{(3)} & n_y^{(3)} \end{bmatrix} \begin{bmatrix} j_x \\ j_y \end{bmatrix}_{(1)}, \\ \begin{bmatrix} j^{(1)} \\ j^{(4)} \end{bmatrix} &= \begin{bmatrix} n_x^{(1)} & n_y^{(1)} \\ n_x^{(4)} & n_y^{(4)} \end{bmatrix} \begin{bmatrix} j_x \\ j_y \end{bmatrix}_{(2)}, \\ \begin{bmatrix} j^{(2)} \\ j^{(3)} \end{bmatrix} &= \begin{bmatrix} n_x^{(2)} & n_y^{(2)} \\ n_x^{(3)} & n_y^{(3)} \end{bmatrix} \begin{bmatrix} j_x \\ j_y \end{bmatrix}_{(3)}, \\ \begin{bmatrix} j^{(2)} \\ j^{(4)} \end{bmatrix} &= \begin{bmatrix} n_x^{(2)} & n_y^{(2)} \\ n_x^{(4)} & n_y^{(4)} \end{bmatrix} \begin{bmatrix} j_x \\ j_y \end{bmatrix}_{(4)}\end{aligned} \tag{9}$$

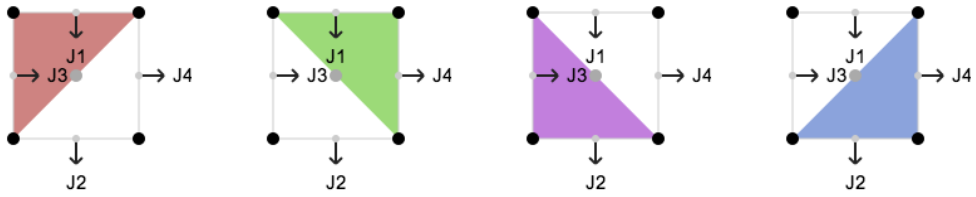

Figure 4: Averaging flux values to a single Cartesian flux for the cell.

Solving Eqn. 9 for each nodal Cartesian flux, $\mathbf{j}^c_{(i)}$, requires inverting a small matrix (2×2 or 3×3) for each node in each cell. Equation 8 can now be discretized by using $\mathbf{j}^c_{(i)} = N^{-1}_{(i)}\mathbf{P}_{(i)}\mathbf{j}$, for simplicity the boundary conditions are

ignored here.

$$\begin{aligned} \mathbf{w}_c^\top v\sigma^{-1}\mathbf{j}_c &= -\phi v(v^{-1}\mathbf{D}_{\text{cell}}\ \text{diag}\left(\mathbf{a}_{\text{cell}}\right)\mathbf{w}) \\ \mathbf{w}^\top\left(\frac{1}{4}\sum_{i=1}^{4}\mathbf{P}_{(i)}^\top\mathbf{N}_{(i)}^{-\top}v\sigma^{-1}\mathbf{N}_{(i)}^{-1}\mathbf{P}_{(i)}\right)\mathbf{j} &= -\mathbf{w}^\top\ \text{diag}\left(\mathbf{a}_{\text{cell}}\right)\mathbf{D}_{\text{cell}}^\top\phi \end{aligned} \tag{10}$$

Where v is the cell volume and the vector $\mathbf{a}_{\text{cell}}$ is the cell surface areas; $\mathbf{P}_{(i)}$ is a projection from $\mathbf{j}$ on the cell faces to the appropriate two fluxes used in $\mathbf{N}_{(i)}^{-1}$. Noticing that this works for any general face function, we can now eliminate the $\mathbf{w}^\top$ and define the mass matrix for this cell.

$$\mathbf{M}_f(\sigma^{-1})_{\text{cell}} = \frac{1}{4}\left(\sum_{i=1}^{4}\mathbf{P}_{(i)}^\top\mathbf{N}_{(i)}^{-\top}v\sigma^{-1}\mathbf{N}_{(i)}^{-1}\mathbf{P}_{(i)}\right) \tag{11}$$

The mass matrix can be created for each cell, and then projected and added to a full mass matrix for the entire mesh, $\mathbf{M}_f(\sigma^{-1})$. It should be noted that it is possible to solve for the average $\mathbf{j}_c$ using a pseudo-inverse of all face normals of each cell at one time.

$$\begin{bmatrix} J^{(1)} \\ J^{(2)} \\ J^{(3)} \\ J^{(4)} \end{bmatrix} = \begin{bmatrix} n_x^{(1)} & n_y^{(1)} \\ n_x^{(2)} & n_y^{(2)} \\ n_x^{(3)} & n_y^{(3)} \\ n_x^{(4)} & n_y^{(4)} \end{bmatrix} \begin{bmatrix} J_x \\ J_y \end{bmatrix} \tag{12}$$

Using this way of finding the Cartesian fluxes leads to $\mathbf{M}_f(\sigma^{-1})_{\text{cell}} = \mathbf{N}^{\dagger^\top}v\sigma^{-1}\mathbf{N}^\dagger$, and can be seen as averaging and then squaring rather than squaring then averaging as before. This version leads to a null space in the mass matrix, making it non-invertible; this can be demonstrated by a simple example: $(\frac{1}{2}(1-1))^2 = 0$ versus $\frac{1}{2}((1)^2+(-1)^2) = \frac{1}{2}$.

The DC resistivity equations are now fully discretized and can be combined into a symmetric positive definite matrix equation.

$$\begin{aligned} \mathbf{M}_f(\sigma^{-1})\mathbf{j} - \mathbf{A}\mathbf{D}^\top\boldsymbol{\phi} &= 0 \\ \mathbf{V}^{-1}\mathbf{D}\mathbf{A}\mathbf{j} &= \mathbf{s} \end{aligned} \tag{13a}$$

$$\begin{bmatrix} \mathbf{M}_f(\boldsymbol{\sigma}^{-1}) & -\mathbf{A}\mathbf{D}^\top \\ -\mathbf{D}\mathbf{A} & 0 \end{bmatrix} \begin{bmatrix} \mathbf{j} \\ \boldsymbol{\phi} \end{bmatrix} = \begin{bmatrix} 0 \\ -\mathbf{V}\mathbf{s} \end{bmatrix} \tag{13b}$$

Note here that this is a saddle point system that can be difficult to solve because $\mathbf{M}_f(\boldsymbol{\sigma})$ is not easily inverted. When the mesh is rectangular, however, $\mathbf{M}_f(\boldsymbol{\sigma}^{-1})$ becomes diagonal, and $\mathbf{j}$ can be eliminated. The formulation of the DC resistivity equations will be used in an example in Section 4. To motivate the following section, the example problem will be geophysical EM using Maxwell's equations.

3.3 Curl

Electromagnetic methods are commonly used in geophysical exploration and monitoring. Maxwell's equations will motivate the discretization of the curl, and will guide the discussion on edge inner products in Sec. 3.4. In the frequency domain, under the quasi-static approximation Maxwell's equations are:

$$\imath\omega\vec{B} + \nabla\times\vec{E} = 0 \tag{14a}$$

$$\nabla\times\mu^{-1}\vec{B} - \sigma\vec{E} = \vec{s} \tag{14b}$$

Where $\vec{E}$ is the electric field, $\vec{B}$ is the magnetic flux, σ again is the conductivity, and μ is the magnetic susceptibility. For discretizing Maxwell's equations we put the electric field on the edges, the magnetic flux on the faces, and electrical conductivity as a cell centered variable. With these definitions, the only operator that must be discretized is the curl, much like the divergence operator we rely on the geometric interpretation of the curl:

$$(\nabla\times\vec{E},\vec{n}) = \lim_{A\to 0}\left(\frac{1}{|A|}\oint_C\vec{E}\cdot dr\right) \tag{15}$$

Where, $\vec{n}$ is the outward facing normal, A is the area of the face, and the line integral direction C is oriented positively with respect to the normal. Figure 5 shows the integrating directions for a unit cube in each unit direction. To discretize

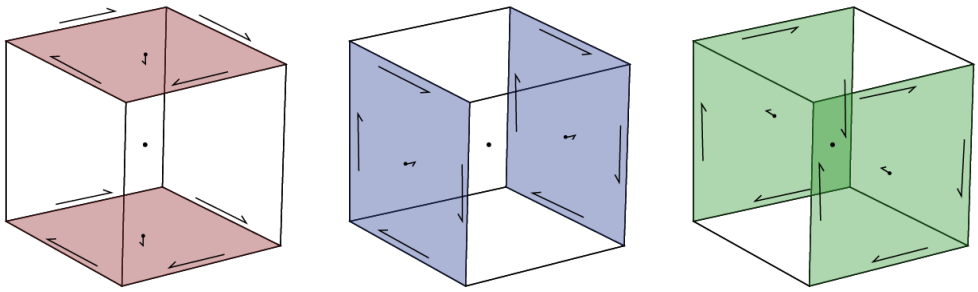

Figure 5: Edge path integration for definition of the curl operator.

the curl of an edge variable, we must integrate along each edge in the appropriate direction (i.e. multiply by ± 1) and divide by the face area.

$$\mathbf{curl}_e \mathbf{E} = \mathsf{diag}\left(\mathbf{a}\right)^{-1} \mathbf{D}\, \mathsf{diag}\left(\mathbf{l}\right) \mathbf{E} \tag{16}$$

Where $\mathbf{l}$ is an edge length vector, and $\mathbf{a}$ is the face area vector. The numeric curl on edges yields a vector variable on cell faces. Similar to the divergence operator, this definition can exploit the logic orthogonality of the mesh and create the difference matrix, $\mathbf{D}$, using Kronecker products. The curl of the magnetic flux ($\mathbf{B}$), which lives on the faces, can be computed using the adjoint of the edge curl up to boundary conditions.

3.4 Edge inner products

When moving to the deformed mesh we again must be sure that the curl is working in Cartesian coordinates. To ensure this we can again integrate with a general face function $\vec{W}_f$ or general edge function $\vec{W}_e$.

$$\int_V \left(\imath\omega\vec{B}, \vec{W}_f\right) dV + \int_V \left(\nabla \times \vec{E}, \vec{W}_f\right) dV = 0 \tag{17a}$$

$$\int_V \left(\nabla \times \mu^{-1}\vec{B}, \vec{W}_e\right) dV - \int_V \left(\sigma\vec{E}, \vec{W}_e\right) dV = \int_V \left(\vec{s}, \vec{W}_e\right) dV \tag{17b}$$

This integration is completed over every cell in the mesh. Equation 17a uses a face function, and can simplify as before to using the mass matrices ($\mathbf{M}_f$) for the face inner product.

$$\imath\omega\mathbf{M}_f\mathbf{b} + \mathbf{M}_f\mathbf{curl}_e\mathbf{e} = 0 \tag{18}$$

This equation, can further simplify as $\mathbf{M}_f$ is invertible and can be eliminated. Equation 17b uses a edge function and requires slight differences from the calculation of the face inner product. Instead of using the normals at each node, the Cartesian edge values, $\mathbf{e}^c_{(i)}$, are projected using the tangents.

$$\mathbf{e}^c_{(i)} = \mathbf{T}^{-1}_{(i)}\mathbf{P}_{(i)}\mathbf{e} \tag{19}$$

where i indicates the node, and $\mathbf{P}_{(i)}$ is the projection matrix that selects the neighboring edges to each node. The inner product is again completed by the mass matrix acting on the edges:

$$\mathbf{M}_e(\sigma)_{\text{cell}} = \frac{1}{n}\left(\sum_{i=1}^{n} \mathbf{P}^\top_{(i)}\mathbf{T}^{-\top}_{(i)} v\sigma \mathbf{T}^{-1}_{(i)}\mathbf{P}_{(i)}\right) \tag{20}$$

where n is the number of nodes (8 in 3D, 4 in 2D). By substituting in the Cartesian field into Equation 17b we can obtain the following system of equations.

$$\begin{bmatrix} \imath\omega & \mathbf{curl}_e \\ \mathbf{curl}_f\mathbf{M}_f(\mu^{-1}) & -\mathbf{M}_e(\sigma) \end{bmatrix} \begin{bmatrix} \mathbf{b} \\ \mathbf{e} \end{bmatrix} = \begin{bmatrix} 0 \\ \mathbf{M}_e\mathbf{s} \end{bmatrix} \tag{21}$$

We can eliminate $\mathbf{b}$, and solve directly for the electric field:

$$\begin{aligned} \mathbf{b} &= -\frac{1}{\imath\omega}\mathbf{curl}_e\mathbf{e} \\ \left(\mathbf{curl}_f\mathbf{M}_f(\mu^{-1})\mathbf{curl}_e + \imath\omega\mathbf{M}_e(\sigma)\right)\mathbf{e} &= -\imath\omega\mathbf{M}_e\mathbf{s} \end{aligned} \tag{22}$$

Note here that we can avoid the saddle point system in this case, which makes the solving of this system less computationally expensive. This formulation of Maxwell's equations will be used in Section 4 to solve a geophysical EM problem.

3.5 Notes on Volume and Area Calculations

The volume and area calculations on the nodal grid are straight forward in two dimensions. However, in three dimensions the faces of the cell may not lie on a plane, and as a result both the volume and face areas are not well defined. For face area, we use the average of the four parallelograms calculated at each node of the face. As seen in Figure 6, the cell volume is calculated by dividing the cell into five tetrahedrons and calculating the volume of each. This way of calculating volumes is more indicative of a twisted mesh, as it is more likely to be negative than the average of eight parallelepipeds.

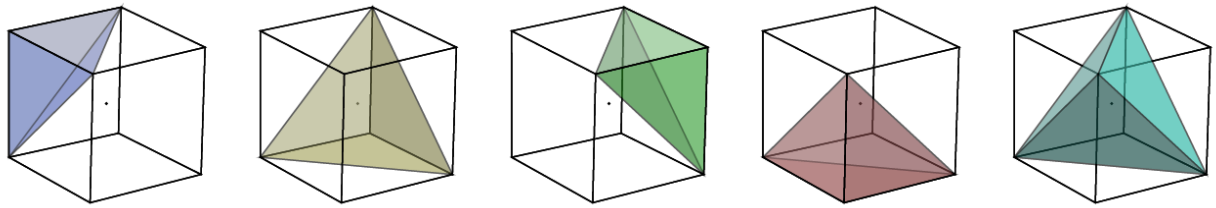

Figure 6: Volume calculation using five tetrahedra.

3.6 Testing

For the logically orthogonal mesh, each of the geometric functions is tested to analytic formulas for simple geometries. Both the face and edge inner product codes have been tested on randomly generated meshes, for integration of a function on the unit cube. In addition to these tests, we use a fictitious source experiment to rigorously test the code for both the EM and DC examples; these experiments converge at $\mathcal{O}(h^2)$ as expected.

4 Geophysical Applications

4.1 DC resistivity

The DC resistivity problem is governed by Poisson's equation with appropriate boundary conditions applied

$$\nabla \cdot (-\sigma \nabla \phi) = \mathrm{I}(\delta(\vec{r} - \vec{r}_{s+}) - \delta(\vec{r} - \vec{r}_{s-})) \tag{23}$$

where σ is the conductivity structure of a medium; ϕ is the electrical potential field induced by a dipole; and I is the electrical current from a dipole. The dipole is represented by two dirac delta functions centered on the positive and negative source locations ($\vec{r}_{s+}$ and $\vec{r}_{s-}$ respectively) [*Pidlisecky et al.*, 2007]; where $\vec{r}$ is a position vector. Neumann boundary conditions are often applied at infinity or sufficiently far from the area of interest in a discretized model [*Haber*, 2011]. These boundary conditions are representative of a field experiment where the site is unbounded.

A forward modeling code was written for a logically orthogonal mesh over a unit cube with Neumann boundary conditions. The forward operators were tested for analytical potential fields with the appropriate boundary conditions. A series of electrode arrays (surveys) were written to produce and collect data from the forward model; the survey used in this paper considered all receiver permutations in a grid on the top surface of the model. It is noted that it is

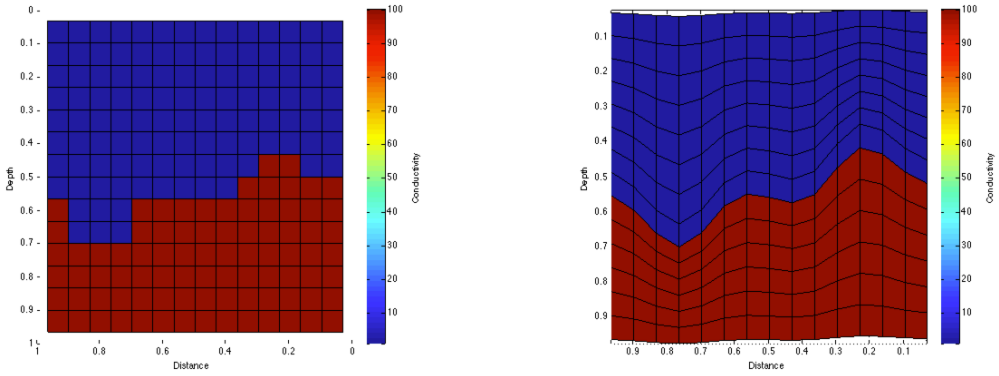

Figure 7: Regular mesh and mesh aligned to layer for a simple conductivity model at $14 \times 14 \times 14$.

not possible experimentally to collect data at the same location as the source electrodes, and these permutations were discarded.

For the numerical experiments presented here we use a true model with a geologic interface with varying elevation. A cross section through the model at a mid-range discretization is seen in Figure 7. The layer above the interface had a conductivity of 1 Sm^{-1}, below the interface had a conductivity of 100 Sm^{-1}. Data was produced from the forward operator using the true model discretized using $45 \times 45 \times 45$ cells. A series of models were created that ranged from $5 \times 5 \times 5$ to $40 \times 40 \times 40$ over the same domain. At each discretization level, the true model down-sampled onto a regular mesh as well as a logically orthogonal mesh that was aligned to the interface. The survey setup was a grid of 4×4 equally spaced electrodes centered on the top surface of the model. There were a total of 16 electrodes, 120 source configurations, and 91 active measurements per source dipole. This gave rise to 10 920 total measurements half of which are symmetric and likely would not have been collected in a field experiment, but were collected in this numerical experiment. The data collected from each of the test models is directly compared to the large model's data and the norm is plotted in Figure 8. The mesh that is aligned to the layer performs significantly better at lower discretizations. For example, at a norm data error of 10^0 the mesh aligned to the layer needed 16^3 cells versus 27^3 when a rectangular discretization was used. The large changes in error at coarse discretizations is likely due to the low accuracy in modeling the location of the sources and receivers.

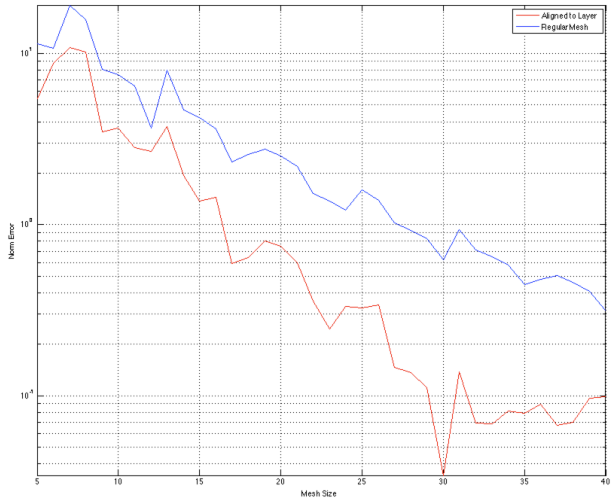

Figure 8: Comparison of norm data error for the regular mesh and the mesh aligned to the interface.

4.2 Geophysical EM

To investigate padding to infinity we will use the geophysical EM problem. Maxwell's equations in the frequency domain are [*Ward and Hohmann*, 1988]:

$$\imath\omega\vec{B} + \nabla \times \vec{E} = 0 \tag{24a}$$

$$\nabla \times \mu^{-1}\vec{B} - \sigma\vec{E} = \vec{s} \tag{24b}$$

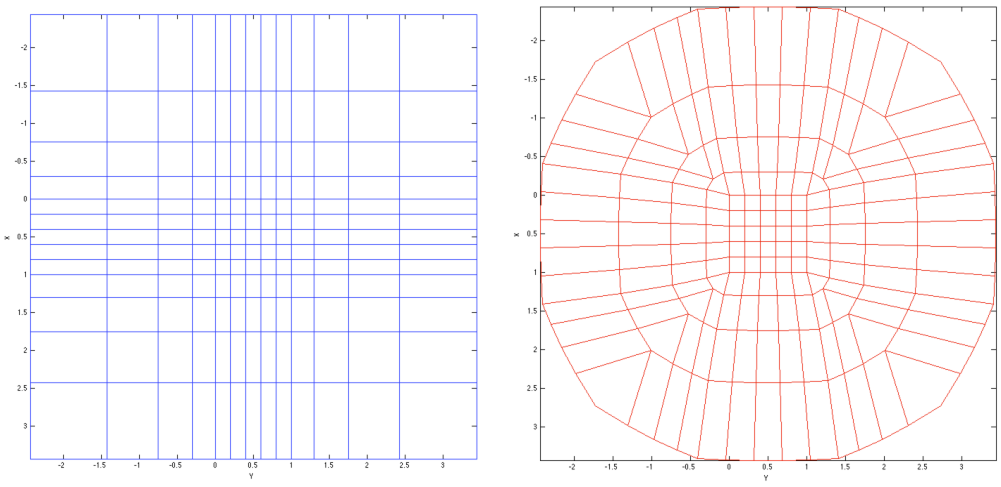

(a) Regular padded mesh (b) Deformed padded mesh

Figure 9: Padding the mesh to infinity using a regular mesh or a deformed mesh.

In this example we will use a magnetic source from a current loop, which is common in geophysical airborne EM surveys. The magnetic source can be approximated by a magnetic dipole that has the same moment and orientation as the loop; this approximation is suitable when the distance from the dipole exceeds that of the actual loop [*Griffiths*, 1999]. The discrete vector potential, $\mathbf{A}$ is defined on cell edges:

$$\mathbf{A} = \frac{m}{4\pi\mathbf{r}^3}\left(-\mathbf{y}\hat{x} + \mathbf{x}\hat{y}\right) \tag{25}$$

Where m is the magnetic moment of the dipole; $\hat{x}$ and $\hat{y}$ are direction vectors; and $\mathbf{r}$ is the radius from the dipole. In this case the dipole is oriented vertically. The source can be constructed by discretely taking the curl of the vector potential [*Ward and Hohmann*, 1988], which is important to produce a source vector that is numerically divergence free.

$$\mathbf{s} = \mathbf{curl}_f\mathbf{curl}_e\mathbf{A} \tag{26}$$

The source can be compared to the analytic solution in a whole space, and the effect of padding on the mesh can be lightly compared. For the whole-space solution of a magnetic dipole we use the formulation in *Ward and Hohmann* [1988] (Page 176):

$$\vec{E} = \frac{\imath\omega\mu m}{4\pi r^2}\left(\imath kr + 1\right)\mathbf{e}^{-\imath kr}\left(\frac{z}{r}\hat{y} - \frac{y}{r}\hat{z}\right) \tag{27a}$$

$$\vec{H} = \frac{m}{4\pi r^3}\mathbf{e}^{-\imath kr}\left[\left(\frac{x^2}{r^2}\hat{x} + \frac{xy}{r^2}\hat{y} + \frac{xz}{r^2}\hat{z}\right)\left(-k^2r^2 + 3\imath kr + 3\right) + \left(k^2r^2 - \imath kr - 1\right)\hat{x}\right] \tag{27b}$$

Where $k = \sqrt{-\imath\mu\sigma\omega}$, in this case the $\hat{x}$ direction is aligned with the positive dipole direction. Having now an analytic and numeric way to solve the full-space response, we can lightly compare the effect of padding to infinity. The biggest problem, with this comparison is that the domain of the experiment changes as seen in Figure 9. The regular mesh padding (Figure 9(a)) has large aspect ratio changes and areas of unnecessary detail far from the area of interest, additionally the distance from the source (in the center of the core-mesh) to the edge of the domain varies with

direction. The logically orthogonal mesh, in Figure 9(b), is a first attempt at alleviating some of the problems with the regular mesh. This mesh is padded inside an approximate sphere (or circle in 2D), has larger cells at distance and as such less aggressive aspect ratio changes within and between neighboring cells. The mesh is created by expanding the mesh sides using a radial vector field where the magnitude and direction of the field can be edited to produce various padding regimes. The method of padding does not create cells of equal volume at each layer, and aspect ratios of cells are not considered in this implementation. In future work, the creation of the mesh using optimized techniques is highly recommended.

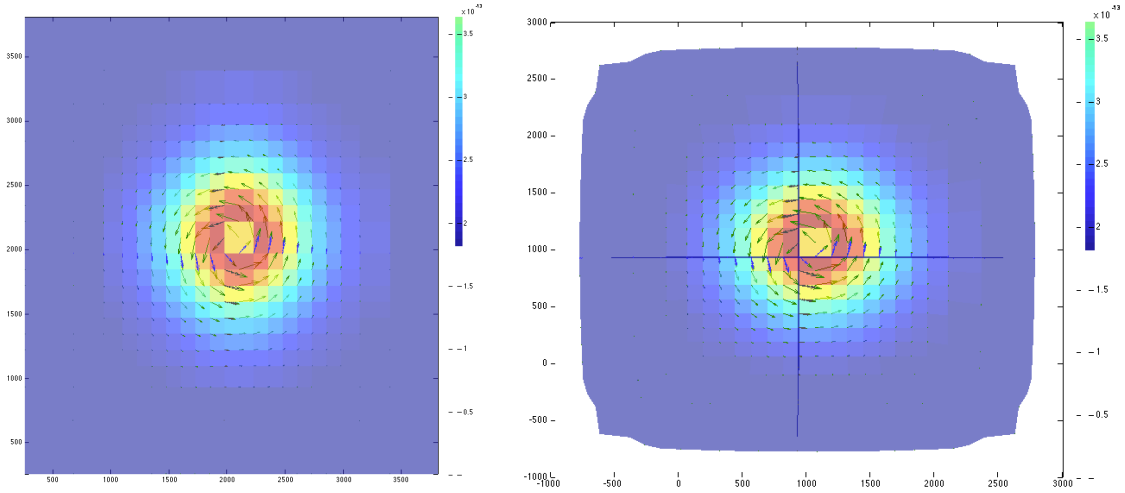

(a) Regular padded mesh

(b) Deformed padded mesh

Figure 10: Electric field response to a magnetic dipole on a regular mesh and a deformed mesh.

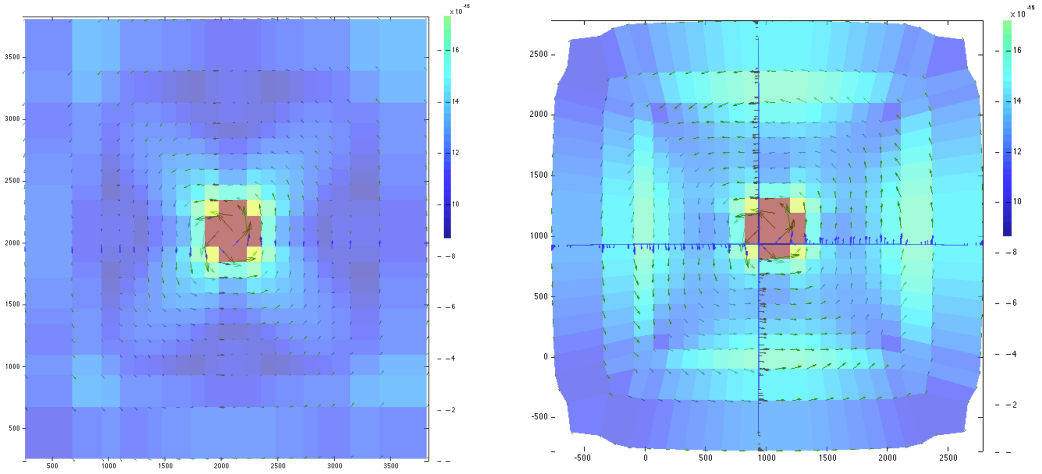

(a) Regular padded mesh

(b) Deformed padded mesh

Figure 11: Residual of electric field (numeric - analytic) on a regular mesh and a deformed mesh.

The results of simulating the electromagnetic response to a dipole in a full-space ($\sigma = 1\text{Sm}^{-1}$) is seen in Figure 10. In both cases the vector field curls around the magnetic dipole as expected. The color is the magnitude of the field, while the arrows show the direction. The residual from the analytic response of a dipole is seen in Figure 11. Here we see that near to the source the numerical solution does not approximate the analytic response, however, as you move

away from the source the response is closer to the analytic. In the regular mesh, there are some errors introduced by the padding, however, these seem to be minimal in comparison with the residuals presented in Figure 11(b) for the circular padding. These preliminary results do not indicate benefit from using the padding scheme of the logically orthogonal mesh. However, more work should be done to confirm results in a more realistic setting where boundary conditions may not play such an important role. Additionally, comparing to the analytic solution may not be the most appropriate test, where as comparing to collected data may prove a better experiment. Additional work should look into better optimized methods to pad the mesh that hold volume or aspect-ratio constant.

5 Conclusions

Using a logically orthogonal mesh for geophysical applications could prove useful for increased accuracy in simulation of topography as well as appropriating infinity. We have presented a general finite volume discretization of the mesh in two and three dimensions. Two model geophysical problems were used to demonstrate the use of the logically orthogonal mesh. The DC resistivity problem demonstrated that aligning the mesh to a layer can significantly improve accuracy at a coarse discretization. Padding to infinity was briefly tacked via the geophysical EM problem. It was found that the simple methods used to create the mesh were not adequate to reduce the discretization error associated with infinity.

The logically orthogonal mesh allows increased degrees of freedom when placing the nodes of the mesh. In simple situations it is possible to significantly improve accuracy of the numerical model at reduced computational costs. However, the increased freedoms in picking node locations forces additional thought in mesh creation and alignment. These issues of mesh creation can be complex problems, and must be handled appropriately. It is suggested that simple meshes (i.e. regular) be used when possible and only use the logically orthogonal mesh when known layers, such as topography, are well defined and known to significantly influence the solution of the problem and data collected. More work should be completed on padding to infinity in a rigorous and optimized framework.

Acknowledgments

Eldad Haber provided invaluable guidance and insight into the discretization of the logically orthogonal mesh.

References

Griffiths, D. J., *Introduction to Electrodynamics*, 3 ed., Prentice Hall, New Jersey, 1999.

Haber, E., *Computational Methods for Simulation Based Optimization*, UBC Math, 2011.

Hyman, J., J. Morel, M. Shashkov, and S. Steinberg, Mimetic finite difference methods for diffusion equations , pp. 333–352, 2002.

Pidlisecky, A., E. Haber, and R. Knight, RESINVM3D : A 3D resistivity inversion package, *Geophysics*, *72*(2), H1–H10, 2007.

Ward, S. H., and G. W. Hohmann, Electromagnetic theory for geophysical applications, *Electromagnetic methods in applied geophysics*, *1*, 131–311, 1988.